JOURNAL OF AIRCRAFT
Vol. 44, No. 3, May–June 2007

Unstable, Cyclically Symmetric and Stable, Asymmetric Pumpkin-Balloon Configurations

Frank Baginski*
George Washington University, Washington, D.C. 20052
Kenneth A. Brakke†
Susquehanna University, Selinsgrove, Pennsylvania 17870
and
Willi W. Schur‡
Accomac, Virginia 23301

DOI: 10.2514/1.20874

By design, a pumpkin balloon is intended to assume a cyclically symmetric "pumpkin-like" shape once it reaches float altitude and is fully inflated. Recent work by the authors showed that under certain circumstances, a strained, cyclically symmetric, pumpkin-balloon configuration can be unstable. This means that the balloon must assume an alternate, noncyclically symmetric, stable-equilibrium shape. Julian Nott's round-the-world balloon Endeavour was one of the first pumpkin-type balloons to encounter this instability. In this paper, we will explore the phenomena of unstable, cyclically symmetric and stable, asymmetric pumpkin-balloon configurations. Through numerical computations using our mathematical model for strained balloon shapes, we find asymmetric equilibria that bear a striking resemblance to those observed in the ground inflation tests of the Endeavour. One difficult aspect of modeling such configurations is dealing with the problem of self-contact. By including certain linear constraints in our variational formulation of the problem, we are able to represent balloon configurations with significant regions of self-contact in a way that mimics how a real balloon stores excess material. We apply our finite element model for strained balloon shapes to Endeavour-like pumpkin balloons and compute a number of asymmetric-equilibrium balloon configurations.

I. Introduction

IN THE late 1980s, in the race for the first balloon circumnavigation of the globe, Julian Nott proposed a design that was radically different from his competitors. Nott's design was a constant-bulge-angle pumpkin balloon called the Endeavour. The constant-bulge-angle pumpkin is described in Sec. II. The Endeavour was a high-pressure balloon that was originally designed to have 64 gores. The Endeavour did not attain its intended cyclically symmetric equilibrium configuration in its first inflation test on the ground. In fact, when the Endeavour was pressurized, it assumed the shape seen in Fig. 1a. Nott and his team surmised that the problem was related to excess material. When two gores were removed, the asymmetry was less severe, but still remained (see Figs. 1b and 1c). Only when four gores were removed did it attain an equilibrium configuration that, at least to the eye, appeared to be cyclically symmetric (see Fig. 1d). Although reducing the number of gores to 60 enabled the balloon to deploy, it is not clear how this balloon would behave over time under normal loading conditions. Nevertheless, the Endeavour was later flown at reduced capacity, though not in a circumnavigation (see Fig. 2).

Even though it was limited to hydrostatic pressure only, Calledine [1] devised a model that attempted to explain the behavior of the fully inflated Endeavour in terms of stability. Being limited by computational capabilities of the time, Calledine cleverly observed that in his semi-empirical approach, he could ignore the variation in the strain energy contribution to the corresponding variation of the total potential energy. This allowed him to approximate the principle of minimum total potential energy by a maximum volume rule. Calledine's approximation, even though formulated on the basis of a simple proxy problem, seems to be remarkably accurate. When we compare our stability results on constant-bulge-angle pumpkin balloons using our full model with the stability results of Calledine, we find very good agreement, supporting Calledine's rationale to ignore strain energy contributions in the analysis of Endeavour-like balloons (see Sec. V). The authors in [2] considered constant-bulge-radius pumpkin balloons. Similar to Calledine, they only considered the hydrostatic pressure, ignoring structural weight and strain energy distributions to the total potential energy. As our analysis in Sec. V shows, ignoring the strain energy is a valid assumption for the limited class of balloon designs considered in [1,2]. However, this assumption would be grossly in error if the structural materials were undergoing large elastic strains, as with balloons made of elastomeric materials. Furthermore, this simplification is also inappropriate when the materials undergo significant viscoelastic deformation over the service life of the balloon, as will be the case in NASA's ultra-long-duration balloon (ULDB), currently under development. NASA's current design scheme for the ULDB uses a trilaminate polyethylene film. At maximum internal pressure and temperature during overflight periods over hot deserts in the southern hemisphere, the film will accumulate significant creep. Clearly, stability analyses need to be performed on the deformed equilibrium state. In the case of viscoelastic materials, this may mean that several equilibrium states need to be examined unless a single equilibrium state can be clearly defined as the most vulnerable to instability.

Analyses are only performed on idealized models. Actual systems are only approximated by such models. Fabrication imperfections and variability in material properties are generally random, and so including them in analytical models is impractical. It is therefore necessary that actual designs fall well inside the stable regime of the feasible design space for a given design class, with sufficient margins

Presented as Paper 7446 at the AIAA 5th Aviation, Technology, Integration, and Operations Conference, 16th Lighter-than-Air and Balloon Systems Conference, Crystal City, VA, 26–29 September 2005; received 3 November 2005; revision received 3 January 2006; accepted for publication 12 January 2006.

*baginski@gwu.edu. Senior Member AIAA.
†brakke@susqu.edu.
‡P.O. Box 698; pwschur@verizon.net. Senior Member AIAA.

a) 64 gores **b) Two gores removed**

c) Two gores removed **d) Four gores removed**

Fig. 1 Inflation tests involving the Endeavour.

for the stability threshold. This issue will require analytical study. Obviously, trial and error by designing, fabricating, and testing is impractical.

The constant-bulge-angle assumption in a pumpkin-balloon design is a geometrically imposed condition and is not based on global equilibrium principles. It merely facilitates generating a three-dimensional pumpkinlike shape. Although some of these designs turn out to be stable, most are unstable. The constant-bulge-radius pumpkin balloon model presented in [3] is based on an approximation to equilibrium that includes weight and pressure variation. Nevertheless, it can also lead to an unstable design under certain circumstances (see Sec. V and the results in [4] for more on the stability of constant-bulge-radius pumpkin balloons). Moreover, because the balloon film is viscoelastic, a balloon that is stable at the start of its mission could, through viscoelastic deformation over time, migrate into a configuration that is unstable (see [4,5] for further discussions on the stability of pumpkin balloons).

In Sec. II, we describe the types of pumpkin balloons that are analyzed in this paper. In Sec. III, we outline our finite element model for strained balloons. In Sec. IV, we define stability as used in our work. In Sec. V, we present numerical studies on the stability of pumpkin-balloon designs. Our analysis predicts that under certain conditions, a cyclically symmetric pumpkin balloon can be unstable, leading one to investigate what configurations such a balloon might assume. In Sec. VI, we consider this question and calculate a number of asymmetric stable-equilibrium shapes related to the unstable Endeavour design. This is a difficult computational problem, because the balloon will have significant regions of self-contact. In Sec. VII, we present concluding remarks.

II. Pumpkin Balloons

In this section, we define the pumpkin balloons that are analyzed in this paper. We begin with a description of a constant-bulge-radius pumpkin that is parametrized as a tubular surface. Next, we consider two pumpkin designs: the Euler-elastica constant-bulge-radius pumpkin balloon and the Euler-elastica constant-bulge-angle pumpkin balloon. The Endeavour was based on the Euler-elastica constant-bulge-angle design.

A. Constant-Bulge-Radius Pumpkin

Let $\boldsymbol{\Upsilon}(s) = R(s)\boldsymbol{i} + Z(s)\boldsymbol{k} \in \mathrm{IR}^3$ be a planar curve that we call the generator of the pumpkin gore. Refer to Fig. 3 for a sketch of a representative Υ drawn in the $y = 0$ plane. A priori $\boldsymbol{\Upsilon}$ is unknown and must be derived from equilibrium conditions. A detailed exposition of the shape-finding equations for a pumpkin balloon, including the determination of $\boldsymbol{\Upsilon}$, is presented in [3].

The generator is parameterized by arc length s (i.e., $|R'(s)|^2 + |Z'(s)|^2 = 1$, where prime denotes differentiation with respect to s). Let $\boldsymbol{t}$ denote the unit tangent and $\boldsymbol{b} = \boldsymbol{t} \times \boldsymbol{j}$ denote the inward unit normal of $\boldsymbol{\Upsilon}$; $\theta = \theta(s)$ is the angle between $\boldsymbol{t}$ and $\boldsymbol{k}$ (see Fig. 3), and

$$\boldsymbol{t}(s) = \sin\theta\boldsymbol{i} + \cos\theta\boldsymbol{k}, \qquad \boldsymbol{b}(s) = -\cos\theta\boldsymbol{i} + \sin\theta\boldsymbol{k}$$

The set $\{\boldsymbol{b}, \boldsymbol{t}, \boldsymbol{j}\}$ gives a right-hand curvilinear basis for IR^3. The curvature of $\boldsymbol{\Upsilon}$ is denoted by κ. We define a tubular surface with generator Υ and constant radius r_B in the following manner. Let

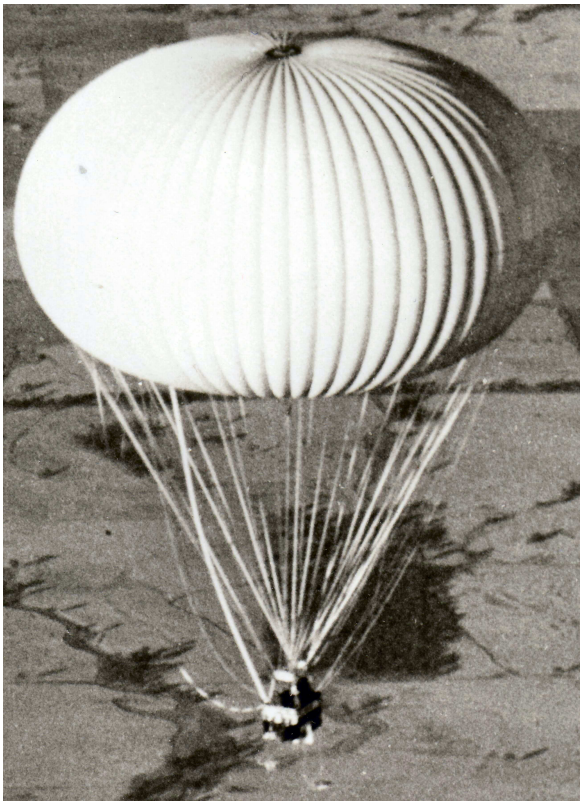

Fig. 2 Endeavour flight at reduced capacity.

$$\begin{aligned} \boldsymbol{x}(s,v) &= (s) + r_B[\boldsymbol{j}\sin v - \boldsymbol{b}(s)\cos v] \\ -\pi < v < \pi, &\qquad 0 < s < L_d \end{aligned} \tag{1}$$

$x(s,v) = \boldsymbol{x}(s,v)\cdot\boldsymbol{i}$, and $y(s,v) = \boldsymbol{x}(s,v)\cdot\boldsymbol{j}$.

We denote partial differentiation using subscript notation (e.g., $\boldsymbol{x}_s = \partial\boldsymbol{x}/\partial s$). By direct calculation, we have

$$\boldsymbol{x}_s(s,v) = [1 + r_B\kappa(s)\cos v]\boldsymbol{t}(s)$$

$$\boldsymbol{x}_v(s,v) = r_B[\boldsymbol{b}(s)\sin v + \boldsymbol{j}\cos v]$$

$$\boldsymbol{x}_s \times \boldsymbol{x}_v = r_B[1 + r_B\kappa(s)\cos v][\boldsymbol{b}(s)\cos v - \boldsymbol{j}\sin v]$$

A unit vector normal to the tubular surface is

$$\boldsymbol{N}(s,v) = \boldsymbol{x}_s \times \boldsymbol{x}_v/|\boldsymbol{x}_s \times \boldsymbol{x}_v| = \boldsymbol{b}(s)\cos v - \boldsymbol{j}\sin v$$

and the triple $\{\boldsymbol{x}_s, \boldsymbol{x}_v, \boldsymbol{N}\}$ gives a right-hand basis for IR^3. The principal curvatures of the tubular surface are

$$\kappa_1(s,v) = \frac{\kappa\cos v}{1 + r_B\kappa\cos v}, \qquad \kappa_2(s,v) = \frac{1}{r_B} \tag{2}$$

A unit tangent to the curve $s \to \boldsymbol{x}(s,v)$ is

$$\boldsymbol{a}_1(s,v) = \boldsymbol{x}_s(s,v)/|\boldsymbol{x}_s(x,v)| = \boldsymbol{t}(s)$$

and a unit tangent to the curve $v \to \boldsymbol{x}(s,v)$ is

$$\boldsymbol{a}_2(s,v) = \boldsymbol{x}_v(s,v)/|\boldsymbol{x}_v(s,v)| = \boldsymbol{b}(s)\sin v + \boldsymbol{j}\cos v$$

where $\boldsymbol{t}$ and $\boldsymbol{b}$ are as previously defined. Note that $\partial\mathbf{a}_2/\partial v = \boldsymbol{b}(s)\cos v - \boldsymbol{j}\sin v = \boldsymbol{N}$. Arc length in the tubular surface along a curve parallel to the generator $s \to \boldsymbol{x}(s,v)$ is $\bar{s}$, where $\mathrm{d}\bar{s} = [1 + r_B\kappa(s)\cos v]\,\mathrm{d}s$.

A pumpkin gore will be a subset of a tubular surface. We assume that the pumpkin gore is situated symmetrically with respect to the x–z plane and interior to the wedge defined by the half-planes $y = \pm\tan(\pi/n_g)x$, with $x \geq 0$. We will refer to r_B as the *bulge radius* of the pumpkin gore. The curve traced by $v \to \boldsymbol{\Upsilon}(s) + r_B[\boldsymbol{j}\sin v - \boldsymbol{b}(s)\cos v]$ is a circle lying in the plane with normal $\boldsymbol{t}(s)$. To find the length of the circular arc that is formed in the pumpkin gore, we need to find the values of v at which this arc intersects the planes $y = \pm\tan(\pi/n_g)x$. For fixed s and $v > 0$, we find that v must satisfy $y(s,v) = \tan(\pi/n_g)x(s,v)$. This leads us to the equation

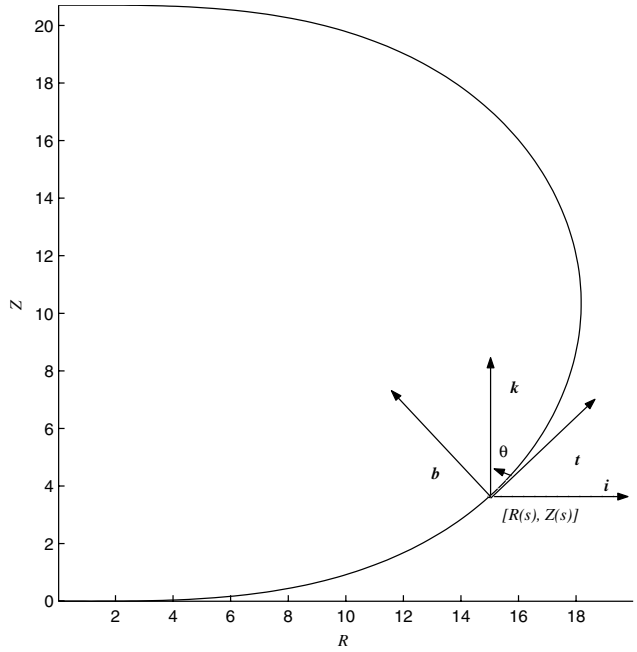

Fig. 3 Pumpkin gore generator $\boldsymbol{\Upsilon}$ parametrized by $[R(s), Z(s)]$ for $0 < s < L_d$ in the $y = 0$ plane; unit vectors $\boldsymbol{t}$, $\boldsymbol{b}$, $\boldsymbol{i}$, and $\boldsymbol{k}$ are indicated; and R and Z are expressed in meters.

$$A(s) + B(s)\cos v + r_B\sin v = 0 \tag{3}$$

where

$$A(s) = -R(s)\tan(\pi/n_g), \qquad B(s) = -r_B\tan(\pi/n_g)\cos\theta(s)$$

Solving Eq. (3) for v, we denote the solution by

$$v_B(s) = v_B[s, n_g, r_B, R(s), \theta(s)]$$

In this paper, $v_B(s)$ is called the *bulge angle* of the constant-bulge-radius pumpkin balloon. The parameter dependence and the dependence on s will be clear from context and so we write $v_B(s)$, for convenience. By symmetry, the solution of Eq. (3) corresponding to the plane $y = -\tan(\pi/n_g)x$ is $v = -v_B(s)$. We define the theoretical three-dimensional pumpkin gore $\mathcal{G}_F$ to be

$$\mathcal{G}_F = \{(x,y,z) = \boldsymbol{x}(s,v), |v| < v_B(s), 0 < s < L_d\}$$

A complete shape $\mathcal{S}$ has cyclic symmetry and is made up of n_g copies of $\mathcal{G}_F$. Note that the length of the centerline of $\mathcal{G}_F$ is

$$L_c = \int_0^{L_d}[1 + r_B\kappa(s)]\,\mathrm{d}s$$

and the length of a tendon is

$$L_t = \int_0^{L_d}\{1 + r_B\kappa(s)\cos[v_B(s)]\}\,\mathrm{d}s$$

Corresponding to $\mathcal{G}_F \subset \mathrm{IR}^3$ is the lay-flat configuration $G_F \subset \mathrm{IR}^2$, shown in Fig. 4. The respective centerlines of $\mathcal{G}_F$ and G_F are isometric. The length of a rib in the spine of $\mathcal{G}_F$ is $2r_Bv_B(s)$ and this is the same as the length of a corresponding segment orthogonal to the centerline of G_F. It follows that the corresponding edge of the lay-flat pattern G_F is longer than the tendon length L_t.

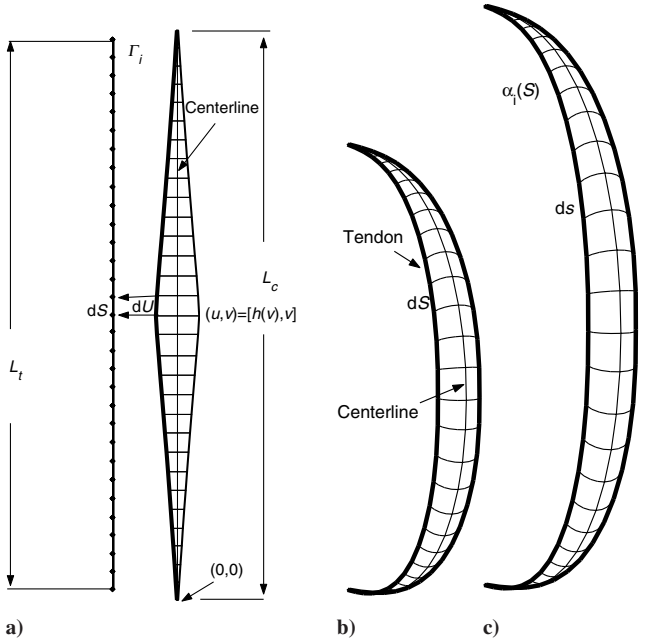

Fig. 4 Discretization of pumpkin gore configurations: a) $G_F \in \mathbf{IR}^2$ is the flat unstrained gore panel with load tendon detached ($0 \le v \le L_c$, where L_c is the length of the centerline; L_t is the tendon length), b) $\mathcal{G}_F \in \mathbf{IR}^3$ is the theoretical pumpkin gore as determined by the shape-finding process (centerlines of G_F and $\mathcal{G}_F$ are identical in length), and c) $\mathcal{S}_F \in \mathbf{IR}^3$ is the deformed pumpkin gore.

B. Pumpkins Based on the Euler-Elastica

If we ignore the film weight density and tendon weight density, assume the differential pressure is constant, and assume zero circumferential stress in the natural shape model, we find that Υ can be related to the Euler-elastica curve, that is,

$$\theta'' + 2\varrho \sin\theta = 0 \tag{4}$$

where $\varrho = \pi p_0/T_0$, p_0 is the constant differential pressure, and T_0 is the total meridional tension [3]. In this case, we find $R(\theta) = \varrho^{-1}\sin(\frac{1}{2}\pi - \theta)$. This connection was first pointed out by Smalley [6] in his discussion of the e-balloon. $Z(\theta)$ can be found using elliptic functions [2] or by directly integrating $Z'(s) = \cos\theta$. The actual length of the generating curve is determined by the Archimedes principle so that the lift generated by the enclosed gas is equal to the weight of the balloon system.

If we assume that the tendon satisfies an equation in the form of Eq. (4), then we are led to a constant-bulge-radius pumpkin balloon that we refer to as the *Euler-elastica constant-bulge-radius* (EECBR) pumpkin. The EECBR is symmetric about its equator and is, in general, slightly taller and slightly wider than the more general constant-bulge-radius pumpkin balloon that was defined at the beginning of this section. Once $\mathcal{G}_F$ is determined, a corresponding lay-flat configuration G_F is determined, as described in the previous section.

Another pumpkin model involving the Euler-elastica is called the *Euler-elastica constant-bulge-angle* (EECBA) pumpkin balloon. In the EECBA pumpkin, one assumes, as we did in the EECBR case, that the tendons follow an Euler-elastica curve. However, the region between adjacent tendons is spanned by circular arcs of constant bulge angle. The Endeavour was an EECBA design. Equations (1) and (2) do not apply to EECBA pumpkin balloons. We will denote the *constant* bulge angle in an EECBA balloon by v_B and the *varying* bulge angle in an EECBR balloon by $v_B(s)$. From context, it will be clear when v_B is constant and when it varies with s. If we compare a constant-bulge-radius pumpkin design with a constant-bulge-angle pumpkin design, we find the constant-bulge-angle pumpkin design leads to a gore pattern that has significantly more gore width material away from the equator and particularly close to the poles (end plates); see Fig. 5 for a comparison of the EECBA and EECBR lay-flat patterns. The EECBA and EECBR balloons corresponding to the gore patterns in in Fig. 5 were designed to lift the same payload. Because of the way in which the respective volumes of the EECBA and EECBR balloons are distributed, the EECBR gore is a bit wider at the equator. In any case, the material distribution in the EECBA pumpkin is problematic, and as a consequence, EECBA pumpkin balloons are more prone to be unstable. In the following, we will be discussing only EECBA and EECBR balloons.

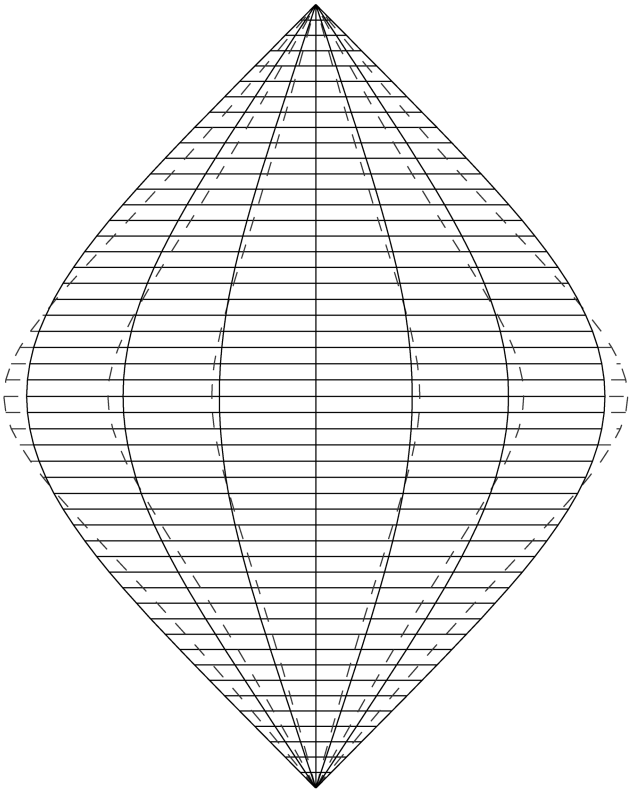

Fig. 5 Euler-elastica lay flat (dashed edges, $r_B = 0.9$) vs Endeavour lay flat (solid edges, $v_B = 75\,\mathrm{deg}$); the Endeavour-like pattern has more material in the midlatitudes; to highlight differences, the figure is not true to scale.

III. Finite Element Model

In this section, we outline the problem of determining the equilibrium shape of a strained balloon. Our model is applicable to any of the pumpkin balloons described in Sec. II. We refer the reader to [7,8] for a more detailed exposition of our finite element model. We will assume that a balloon is situated so that the center of the nadir fitting is located at the origin of a Cartesian coordinate system. The nadir fitting is fixed, and the apex fitting is free to slide up and down the z axis. The nadir and apex fittings are assumed to be rigid.

The reference configuration $\Omega \subset \mathrm{IR}^2$ for a complete balloon $\mathcal{S} \subset \mathrm{IR}^3$ is

$$\Omega = \cup_{i=1}^{n_g} G_i$$

where G_i is isometric to G_F, and G_F is determined by the particular design choice (e.g., Euler-elastica constant-bulge-angle pumpkin or Euler-elastica constant-bulge-radius pumpkin). In this case,

$$\mathcal{S} = \cup_{i=1}^{n_g} \mathcal{S}_i$$

where $\mathcal{S}_i$ is a deformation of G_i. An equilibrium configuration of a fundamental gore is denoted by $\mathcal{S}_F$. For convenience, we assume that the fundamental gore $\mathcal{S}_F$ is situated symmetrically about the $y = 0$ plane and is contained within the wedge-shaped region $|y| \le (\tan\pi/n_g)x$, $x \ge 0$, and $z \ge 0$. If $\mathcal{S}$ is a cyclically symmetric balloon shape with n_g gores, then $\mathcal{S}$ can be generated from n_g copies of $\mathcal{S}_F$,

where the corresponding reference configuration is G_F, which is assumed to be situated with the bottom of G_F centered at the origin of a (u, v) coordinate system (see Fig. 4). The sets Ω and $\mathcal{S}$ are discretized by constant-strain, plane-stress, triangular finite elements. Adjacent gores are joined at their common edge. Tendons are located along the edges at which adjacent gores are joined.

We will describe our model as it applies to a complete balloon. However, at times we will impose certain symmetry conditions, which will reduce the total number of degrees of freedom in our model. For our stability studies, we first compute a cyclically symmetric, strained-equilibrium shape for a fully inflated balloon, but stability of that configuration is calculated for the full balloon. For asymmetric shapes, we use the same model and adjust the boundary conditions appropriately.

The total potential energy $\mathcal{E}$ of a strained inflated balloon configuration $\mathcal{S}$ is the sum of six terms:

$$\mathcal{E}(\mathcal{S}) = \mathcal{E}_P + \mathcal{E}_f + \mathcal{E}_t + \mathcal{E}_{\text{top}} + S_t^* + S_f^* \tag{5}$$

where

$$\mathcal{E}_P = \int_V P(z)\,\mathrm{d}V = -\int_{\mathcal{S}} \left(\frac{1}{2}bz^2 + P_0 z\right)\boldsymbol{k}\cdot\boldsymbol{n}\,\mathrm{d}\sigma \tag{6}$$

$$\mathcal{E}_f = \int_{\mathcal{S}} w_f z\,\mathrm{d}A \tag{7}$$

$$\mathcal{E}_t = \sum_{i=1}^{n_g}\int_0^{L_t} \boldsymbol{\alpha}_i(S)\cdot\boldsymbol{k}\,w_t\,\mathrm{d}S \tag{8}$$

$$\mathcal{E}_{\text{top}} = w_{\text{top}} z_{\text{top}} \tag{9}$$

$$S_t^* = \sum_{i=1}^{n_g}\int_0^{L_t} W_t^*(\epsilon_i)\,\mathrm{d}S \tag{10}$$

$$S_f^* = \int_\Omega W_f^*\,\mathrm{d}A \tag{11}$$

where $\mathcal{E}_P$ is the hydrostatic pressure potential due to the lifting gas, $\mathcal{E}_f$ is the gravitational potential energy of the film, $\mathcal{E}_t$ is the gravitational potential energy of the load tendons, $\mathcal{E}_{\text{top}}$ is the gravitational potential energy of the apex fitting, S_t^* is the total tendon strain energy, and S_f^* is the total film strain energy. For the purpose of the analytical studies in this paper, we assume that the differential pressure is in the form $-P(z) = bz + P_0$, where P_0 is known. $V \subset \mathrm{IR}^3$ is the region enclosed by $\mathcal{S}$, and $\mathrm{d}V$ is the volume measure in IR^3. We follow the convention that $-P(z) > 0$ means that the internal pressure is greater than the external pressure. P_0 is the differential pressure at the base of the balloon for which $z = 0$, b is the specific buoyancy of the lifting gas, $\boldsymbol{n}$ is the outward unit normal, $d\sigma$ is surface area measure in the strained balloon surface, w_f is the film weight per unit area, w_t is the tendon weight per unit length, $\boldsymbol{\alpha}_i \in \mathrm{IR}^3$ is a parametrization of a deformed tendon with reference configuration Γ_i, w_{top} is the weight of the apex fitting, and z_{top} is the height of w_{top}. The strain in the ith tendon is ϵ_i. $W_t^*(\epsilon_i)$ is the relaxed strain energy density in the ith tendon. W_f^* is the relaxed film strain energy density. Relaxation of the film strain energy density is a way of modeling wrinkling in the balloon film and has been used in the analysis of pumpkin-shaped balloons in [7,8].

To determine a strained equilibrium balloon shape, we solve the following:

$$\text{problem } \star \qquad \min_{\mathcal{S}\in\mathcal{C}} \mathcal{E}(\mathcal{S}) \tag{12}$$

where $\mathcal{C}$ denotes the class of feasible balloon shapes. Boundary conditions or symmetry conditions are built into $\mathcal{C}$. In (12), the continuum problem of finding an equilibrium configuration of the balloon is cast as an optimization problem. This approach is particularly well suited for the analysis of compliant structures. Problem $\star$ is solved using Surface Evolver, an interactive software package for the study of curves and surfaces shaped by energy minimization that was developed by the second author [9]. Surface Evolver was used for the analyses presented in [4,5].

Remark: Self-contact of the balloon film is handled by two mechanisms. First, the vertical planes that bound the sides of the balloon segment are symmetry planes of clefts, and these planes are sticky, in the sense that any surface node that hits one of the planes is thenceforth confined to the plane and cannot pass beyond it. Second, clefts between the end planes are handled by checking, for each node at the bottom of a groove (originally the tendon nodes), whether the two short horizontal edges emanating from the node have passed each other. If they have, then the two edges are merged to form one edge, and the merged endpoint is now deemed to be at the bottom of a groove. The second mechanism does not permit opposing films to slide on each other, and so it may introduce some extra strain, but it does not come into play until the perturbations are well-developed, and does not seem to have hindered their development. Unlike other works on this subject in which shapes are not converged solutions and the balloon film is allowed to intersect itself, forming internal gas tubes (e.g., [10]), our approach leads to converged solutions with self-contact, but without self-intersections. Our model leads to a distribution of material that mimics the features of a real asymmetric mode of a pumpkin balloon.

IV. Stability

The degrees of freedom (DOF) in a faceted balloon shape $\mathcal{S}$ are the x, y, and z coordinates of the nodes of triangular facets $\mathcal{T} \in \mathcal{S}$ that are free to move. Let $\boldsymbol{x} = (x_1, x_2, \ldots, x_N)$ be a list of the DOF. Let $\mathcal{E}(\boldsymbol{x})$ be the total energy of a faceted balloon configuration $\mathcal{S} = \mathcal{S}(\boldsymbol{x})$. The gradient of $\mathcal{E}$ evaluated at $\boldsymbol{x}$ is the $1 \times N$ vector:

$$D\mathcal{E}(\boldsymbol{x}) = \left[\frac{\partial \mathcal{E}}{\partial x_j}\right], \qquad j = 1, 2, \ldots, N$$

The Hessian of $\mathcal{E}$ evaluated at $\boldsymbol{x}$ is the $N \times N$ matrix:

$$H_{\mathcal{E}}(\boldsymbol{x}) = D^2\mathcal{E}(\boldsymbol{x}) = \left[\frac{\partial^2 \mathcal{E}}{\partial x_i \partial x_j}\right], \qquad i, j = 1, \ldots, N \tag{13}$$

Although N can be large for a full balloon, $H_{\mathcal{E}}$ is sparse. The lowest eigenvalue of $H_{\mathcal{E}}$ was calculated by inverse iteration. The matrix $H_{\mathcal{E}} - tI$ was sparse Cholesky factored, with the shift value t chosen to guarantee positive definiteness. The factored matrix was then used to iteratively solve $(H_{\mathcal{E}} - tI)\boldsymbol{x}_{n+1} = \boldsymbol{x}_n$, starting with a random vector $\boldsymbol{x}_0$, until the iteration converged, almost certainly producing the eigenvector of the lowest eigenvalue (see Sec. 11.7, p. 493 in [11]). We are led to the following definition of stability.

Definition 4.1: Let $\mathcal{S} = \mathcal{S}(\boldsymbol{x})$ be a solution of problem $\star$. We say $\mathcal{S}$ is stable if all the eigenvalues of $H_{\mathcal{E}}(\boldsymbol{x})$ are positive. We say $\mathcal{S}$ is unstable if at least one eigenvalue of $H_{\mathcal{E}}(\boldsymbol{x})$ is negative. We say that the stability of $\mathcal{S}$ is indeterminate if the lowest eigenvalue of $H_{\mathcal{E}}(\boldsymbol{x})$ is zero.

Remark: Definition 4.1 is related to Lagrange's energy criterion. For elastic bodies under static conservative loads (as is the case in our paper), the energy criterion is almost universally accepted as a method of determining points of instability and the behavior of the structure in a neighborhood of these points. Roughly speaking, one must add energy to displace a body from a stable state (i.e., the change in potential energy is positive for all sufficiently small displacement fields). Conversely, if the change in potential energy is negative for *some* admissible displacement, then the equilibrium state is unstable, and disturbing an unstable equilibrium state releases energy that will be turned into motion (see [12], p. 125–126). For a

nonlinear problem, such as the one we study here, multiple stable equilibria exist. It is not so important to understand the precise mechanism that drives the evolution of a balloon shape to an undesired equilibria. The only desired equilibrium is the cyclically symmetric shape at which the loads are evenly distributed. However, to demonstrate the robustness of our solution process and to compare the shapes predicted by our model with real balloons, we calculate a number of asymmetric equilibria in Sec. VI.

In principle, the fully inflated shape should be cyclically symmetric so that the loads are distributed uniformly over the entire balloon. If we assume a priori that the strained balloon shape is cyclically symmetric, problem $\star$ can be solved for a half-gore, and $\mathcal{S}_F$ is determined. $\mathcal{S}_F$ is indeed a stable local equilibrium within the class of cyclically symmetric shapes. However, within the class of feasible complete balloon shapes, the complete balloon generated by $\mathcal{S}_F$ could turn out to be unstable, as was demonstrated in [5].

V. Parametric Studies

In this section, we will introduce two sets of parameters denoted by $\boldsymbol{p}$ and $\boldsymbol{q}$. Geometry, weight-related, and loading parameters are the elements of $\boldsymbol{p}$, and the elements of $\boldsymbol{q}$ are material properties. The tendon slackness parameter ϵ_t is treated as a material property and is a component of $\boldsymbol{q}$.

The elements of $\boldsymbol{p}$ include parameters that are input into the shape-finding process for an EECBR pumpkin balloon: n_g is the number of gores; r_B is the bulge radius, etc. In the case of an EECBA pumpkin, the bulge angle υ_B is used in place of r_B as a parameter. The Endeavour was an EECBA pumpkin balloon. Complete design specifications for the Endeavour were not available to us, and so we selected materials that are commonly used in the fabrication of NASA ultra-long-duration balloons. For our demonstrations in this paper, we generated EECBA and EECBR designs. For comparisons with the actual Endeavour balloon, we found an Euler elastica with $r_B = 0.979$ m and $n_g = 64$ leads to a bulge angle at the equator of $\upsilon_B = 60$ deg. The Endeavour used a bulge angle of $\upsilon_B = 60$ deg. Nominal parameter values for $\boldsymbol{p}$ are contained in Table 1. Although we assumed $P_0 = 200$ Pa in our studies, the Endeavour (with its stronger balloon fabric and Kevlar tapes) was capable of containing differential pressures on the order of 2 kPa.

Typically, material properties such as the film modulus and Poisson ratio do not enter directly into the shape-finding process. Once a set of values are assigned to $\boldsymbol{p}$, the corresponding pumpkin gore shape $\mathcal{G}_F(\boldsymbol{p})$ is found and the lay-flat pattern $G_F(\boldsymbol{p})$ is determined, along with other quantities such as the total system weight, volume, tendon length, and seam length of the lay-flat gore pattern, as outlined in Sec. II. The three-dimensional shape $\mathcal{G}_F(\boldsymbol{p})$ is discretized into a collection of triangular facets $\mathcal{G}_F(\boldsymbol{x}; \boldsymbol{p})$, which is used as the initial guess for solving problem $\star$ and determining the corresponding strained equilibrium shape of the fundamental gore $\mathcal{S}_F$. Once $\mathcal{S}_F$ is determined, we then use the cyclic symmetry of the balloon to generate a complete shape $\mathcal{S}$ using n_g copies of $\mathcal{S}_F$. A cyclically symmetric complete balloon generated from $\mathcal{G}_F$ will be denoted by $\mathcal{S}_d(\boldsymbol{p})$.

We are most interested in investigating the stability of equilibrium configurations of pumpkin designs as a function of n_g and r_B for EECBR pumpkins and n_g and υ_B for EECBA balloons. For this reason, we define the following family of EECBR pumpkin balloon designs:

$$\Pi_d = \{[\mathcal{S}_d(\boldsymbol{p}), \Omega(\boldsymbol{p})] | \bar{r}_B(n_g) < r_B < \infty\} \tag{14}$$

where $20 \leq n_g \leq 200$, $\bar{r}_B(n)$ is the smallest possible bulge radius for a design with n gores in class Π_d. For EECBR pumpkin balloons, $\bar{r}_B(n) = \max(R)\sin(\pi/n)$. For convenience, we will refer to a particular design in Π_d by indicating the number of gores and the bulge radius. For example, $\Omega(n_g, r_B)$ with $n_g = 64$ and $r_B = 0.979$ m refers to an EECBR pumpkin that is similar in size to the Endeavour.

Table 1 Input parameters for pumpkin shape-finding

Description	Value
Tendon weight density, N/m	0.094
Film weight density, N/m^2	0.344
Constant differential pressure, Pa	200
Film thickness, μm	20.32

Table 2 Material properties for 20-μm-thick polyethylene

Description	Value
Film Young's modulus, MPa	202
Film Poisson ratio	0.830
Tendon stiffness, kN	650

The class of EECBA pumpkin balloon designs is denoted by

$$\Pi'_d = \{[\mathcal{S}_d(\boldsymbol{p}), \Omega(\boldsymbol{p})] | 30\,\text{deg} \leq \upsilon_B \leq 90\,\text{deg}\}$$

where $20 \leq n_g \leq 100$ and υ_B is the constant bulge angle. There was no need to go beyond 100 gores for the EECBA balloons because they were all unstable for $n_g \geq 100$. A lay-flat pattern in the Π'_d family will be denoted by $\Omega(n_g, \upsilon_B)$. The balloon design being discussed will be clear from the context; $\Omega(n_g, \upsilon_B)$ with $(n_g, \upsilon_B) = (64, 60\,\text{deg})$ corresponds closest to the Endeavour.

Once a design has been defined, we can then carry out a stress analysis of that design for some loading conditions. For this analysis, we include the full set of material properties: E_f is film Young's modulus, ν is film Poisson ratio, K_t is tendon stiffness, ϵ_t is tendon slackness, etc. The material properties presented in Table 2 were determined experimentally at room temperature conditions by NASA Goddard Space Flight Center's Wallops Flight Facility balloon lab.

The vector $\boldsymbol{q}$ includes parameters that were not used directly in the shape-finding process. Once $\boldsymbol{p}$ and $\boldsymbol{q}$ are specified, we can proceed to solving problem $\star$ and determining a strained balloon shape. Note that the shape-determination process and the stress-analysis process are separate, and so it is possible to use one value of a parameter in the shape-finding process and another value in the solution of problem $\star$. The shape-finding process defines the lay-flat pattern $\Omega(\boldsymbol{p})$ and provides a three-dimensional shape $\mathcal{S}_d(\boldsymbol{p})$ that is used for initializing the solution process for problem $\star$. The strained equilibrium shape that is a solution of problem $\star$ is denoted by $\mathcal{S}[\boldsymbol{p}, \boldsymbol{q}, \Omega(\boldsymbol{p})]$. After solving problem $\star$ with a design $(\mathcal{S}_d, \Omega) \in \Pi_d$ or $(\mathcal{S}_d, \Omega) \in \Pi'_d$, we will then classify the resulting strained equilibrium configuration according to Definition 4.1.

Remark:

1) The shape-finding process described in Sec. II is based on an approximation to the fully inflated equilibrium shape and includes weight and pressure variation [3]. This approach leads to a gore pattern that is consistent with those used in the manufacture of actual pumpkin balloons. In reality, the film is an elastomer, and so we use a separate process (i.e., the finite element model outlined in Sec. III) for stress analysis. For the finite element analysis to provide meaningful results, the reference configuration (i.e., gore pattern) must be well-defined and consistent with the manufacturing process.

2) We carried out analyses using a complete balloon and compared these to analyses carried out using one half of a balloon, that is, assuming a balloon has one plane of reflectional symmetry. We found that there were roughly twice as many unstable modes for the complete balloon than there were for one half of a balloon. However, after classifying the corresponding designs as stable or unstable, we found both approaches led to roughly the same stability results. This is to be expected, due to symmetry breaking of two-dimensional eigenspaces of the full balloon. Thus, we would arrive at roughly the same unstable region if either a full or half-balloon were analyzed. To reduce computation time, we analyzed a half-balloon in our stability studies.

3) We note that stability of an equilibrium configuration is investigated at a strained equilibrium state. In general, a strained equilibrium shape is only approximately a cyclically symmetric constant-bulge-radius surface. Other strained equilibrium states (due to pressure variations or viscoelastic straining over time) depart from the cyclically symmetric constant-bulge-radius configuration even more. In the case of a viscoelastic film, that departure can be significant. As shown in [5] by way of looking at different classes of balloon designs, this shape change can have a profound effect on stability.

Previous analytical work by the authors showed that for sufficiently small n_g, a minimum bulge radius design that approaches the lower bound is robustly stable. This has been demonstrated through physical testing in the exploratory work [13] for test vehicles with $n_g = 48$ and was demonstrated analytically for even larger n_g in [5]. Calledine [1] showed that for constant-bulge-angle designs, increasing the number of gores increases vulnerability to instability of the cyclically symmetric configuration.

We analyzed EECBA balloon designs in Π'_d for nominal parameter values. The results are shown in Fig. 6a. In Fig. 6, if a design $\Omega(n_g, v_B)$ is unstable, then the point with coordinates n_g and v_B is covered with a small disk. A design that is stable is covered with a circle. We see from Fig. 6a that an EECBA pumpkin balloon with Endeavour-like parameters clearly lies in the unstable region. For comparison purposes, we considered designs in which the nominal gore pattern is widened by 2 cm. The stable and unstable designs are indicated in Fig. 6b. We find that the number of unstable designs increases when the gore width increases. We compared our stability results obtained using our full model [Eq. (5)] with Calledine's [1] model, which only includes hydrostatic pressure. In Fig. 6, we plot two stability curves derived by Calledine, $v_B = (34/n)^{2/5}$ rad (appropriate for a 64-gore design; see Eq. 26 in [1]) and

$$v_B = (47/n)^{2/5} \text{ rad} \tag{15}$$

(appropriate for a 60-gore design; see Eq. 27 in [1]). To facilitate comparisons with Calledine [1], we follow his conventions and convert bulge angle measurements to degrees in Fig. 7. From Fig. 6a, we see that our results on EECBA balloons are in very close agreement with Calledine, supporting his assertion that for constant-bulge-angle designs and small strains, it is appropriate to ignore the film strain energy and load tendon strain energy in a stability analysis of the fully inflated EECBA balloon. Calledine's model does not do so well for the constant-bulge-radius pumpkins (see the next paragraph). Furthermore, large strains whether elastic or viscoelastic, limit the usefulness of Calledine's approach.

We generated Π_d, a class of constant-bulge-radius pumpkin balloons of comparable size to those in Π'_d, and determined the stability of these designs. We found that all designs in Π_d were stable (see Fig. 7a). When we increased the gore width by one centimeter, we found that for $142 \le n_g \le 200$ and $r_B < 0.4$ m, some equilibrium configurations are unstable (see Fig. 7c). Note that even with a 1-cm perturbation, the constant-bulge-radius pumpkin balloons are stable for $n_g < 142$. An EECBR pumpkin balloon similar in size to the Endeavour falls well inside the stable region. In Figs. 7a and 7c, we present our EECBR results in terms of n_g and r_B. For each design in Π_d, we calculated the maximum chord ratio:

$$\Delta = \max_{0 \le s \le L_d} \frac{2 r_B v_B(s)}{2 r_B \sin v_B(s)} \tag{16}$$

where we see that $1 \le \Delta \le \frac{1}{2}\pi$. The maximum value of Δ is taken at the equator, and $v_B(s)$ decreases as one nears the end plates. Stability results are presented in terms of n_g and Δ in Figs. 7b and 7d. In [14], the authors observed relation (16), substituted $v_B = (47/n)^{2/5}$ into it, and then asserted that EECBR designs that fell above the curve $[n, (47/n)^{2/5}/\sin(47/n)^{2/5}]$ were unstable and those that fell below this curve were stable (see Fig. 6 in [14]). This curve is reproduced in Figs. 7b and 7d, which clearly demonstrate that $[n, (47/n)^{2/5}/\sin(47/n)^{2/5}]$ is not a reliable indicator of instability for EECBR balloons. We assert that our model is a better indicator of the stable/unstable boundary for EECBR balloons. This is demonstrated in [4], in which our analytic predictions are compared with available flight data and experimental data, and we find a very good correlation.

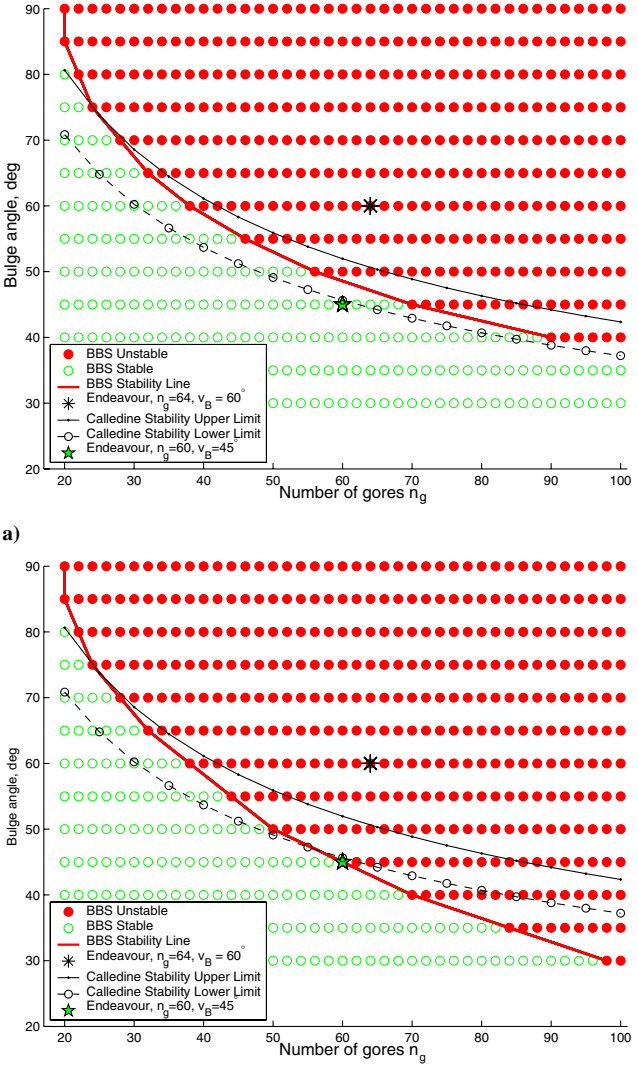

Fig. 6 Stability plots for Euler-elastica constant-bulge-angle balloons: a) case 1, nominal gore width; b) case 2, gore width increased by 2 cm. Calledine [1] stability curves $n < 34/v_B^{5/2}$ and $n < 47/v_B^{5/2}$ are shown. With a 2-cm gore width perturbation, the 60-gore alternate Endeavour design is still on the border of instability. BBS stability is based on Definition 4.1. Although v_B has the unit of radians in our calculations, to facilitate comparisons with Calledine's work, we convert the bulge angle measurements to degrees.

VI. Asymmetric Equilibria

If a cyclically symmetric shape is unstable, an alternate equilibrium configuration must exist. We used Surface Evolver to explore the set of alternative equilibria. We are motivated by the photographs of the Endeavour and the findings in [13] to seek shapes with a certain wave number k. The wave number is the number of waves in a complete balloon, and in this case, we say the shape has $k$fold symmetry. For example, in Figs. 1a–1c, it appears that the Endeavour assumed a shape with $k = 1$. For our case studies, we assumed an EECBA design with $n_g = 64$, $v_B = 75$ deg, and $r_B = 0.848$ m at the equator. Our analysis in Sec. V shows this design to be unstable. To begin our studies, we computed equilibrium configurations for collections of p gores with $p = \frac{1}{2}, 4, 5, \ldots, 11$ (see Table 3). If $2p$ does not divide 64, there is a gap of $r = 64 \pmod{2p}$ gores in the complete balloon, because the collection

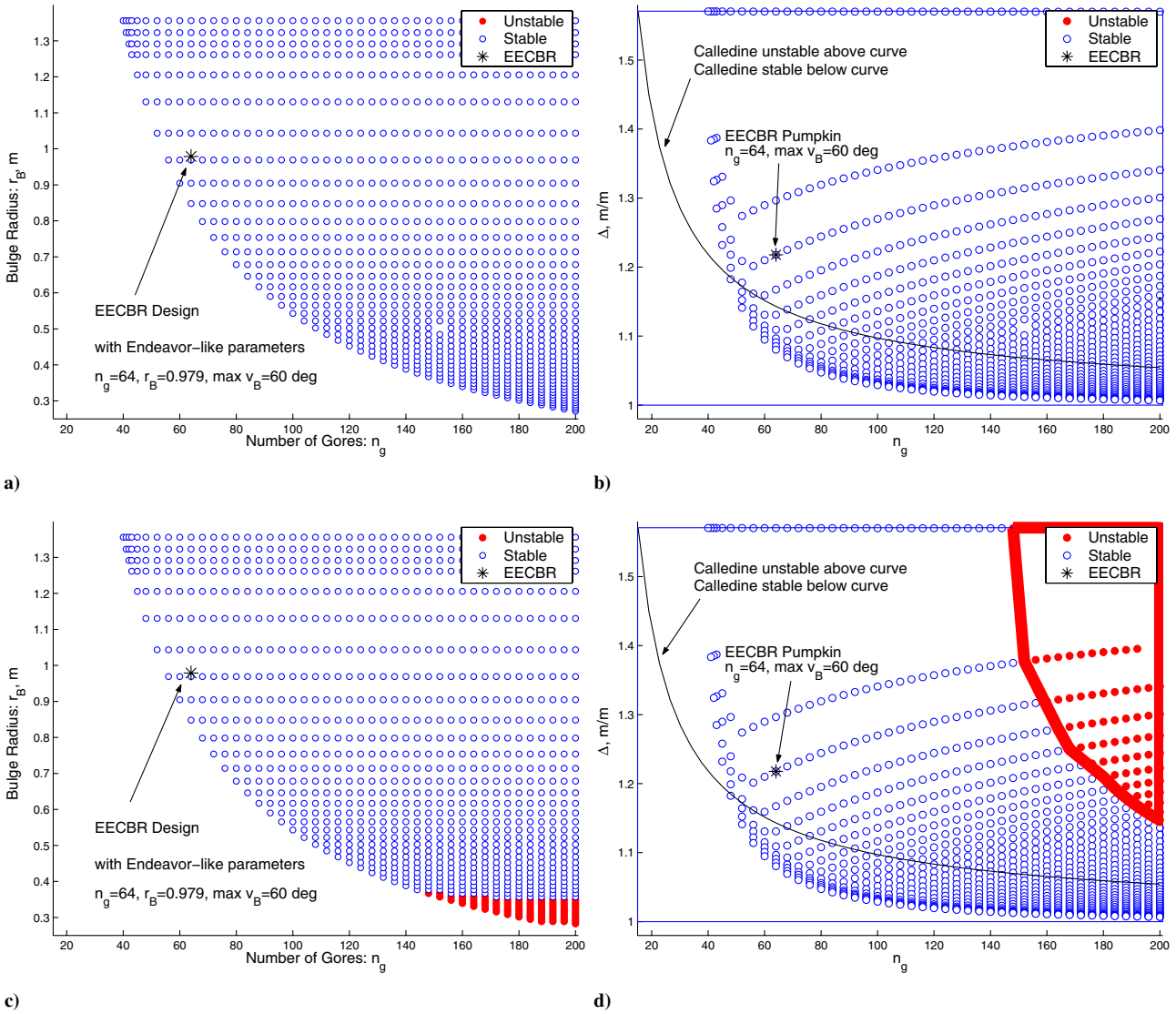

Fig. 7 Stability plots for Euler-elastica constant-bulge-radius balloons: a) nominal gore width, (n_g, r_B) family, all feasible designs are stable; b) nominal gore width, (n_g, Δ) family, all feasible designs are stable; c) gore width increased by 1 cm, (n_g, r_B) family; and d) gore width increased by 1 cm, (n_g, Δ) family.

of p gores does not generate a closed shape. Note that when $p = \frac{1}{2}$, 4 or 8, we find that the collection of p gores generates a complete balloon. An evolved equilibrium configuration of a fundamental section with $p = 4$ is presented in Fig. 8, and the complete balloon is presented in Fig. 9. Our approach to handling self-contact works very well. As Fig. 8 shows, our asymmetric shapes have no "internal tubes" or regions of self-intersection inside the balloon.

For high values of p, the gore structure becomes invisible, and it is possible to compute shapes with wave numbers that are not necessarily divisors of 64. Because it is possible for some tendons that lie in a symmetry plane (where excess film is stored) to become slack or nearly slack, shapes with a variety of wave numbers are not unexpected. For example, to compute a shape with $k = 3$, we use the $p = 10$ solution in Table 3 to generate an initial configuration. To insure that the resulting shape has no gaps, we must work with a minimum of 32 gores. An equilibrium configuration with threefold symmetry is shown in Fig. 10. In this case, we find $E = -6285$ kJ and $V = 15,713$ m^3.

Table 3 Total energy of Endeavour-like balloons with p gores per half-section; S is the cyclically symmetric and $r = 64 \pmod{2p}$ is the number of gores per gap

p	r	E, kJ	V, m^3	Symmetry
1/2	0	−6, 261	15,631	S
4	0	−6, 261	15,631	eightfold/S
5	4	−6, 263	15,650	——
6	4	−6, 270	15,680	——
7	8	−6, 279	15,705	——
8	0	−6, 285	15,719	fourfold
9	10	−6, 288	15,726	——
10	4	−6, 287	15,721	——
11	2	−6, 284	15,713	——

Even though the shapes with fourfold and threefold symmetry have lower energy than the cyclically symmetric shape in Table 3, we do not claim that the balloon will assume either of these configurations or even the one of lowest energy. Shapes with threefold and fourfold symmetry are but two of the possible alternative states that are stable local minima. What we can say is that when the cyclically symmetric shape is unstable, it would be impossible for it to be observed.

Remark: For high values of p, we found that the shapes all developed higher wave instabilities, eventually above the half-wave mode that was being studied. Typically, the magnitude of the half-wave mode got relatively large before the higher-wave-number mode appeared and did not evolve back to the pure higher-wave-number mode. This could have been an artifact of the antipenetration scheme that was implemented.

It is interesting to note that when $p = 4$, the evolved collection of four gores generates a balloon shape with eightfold symmetry that is

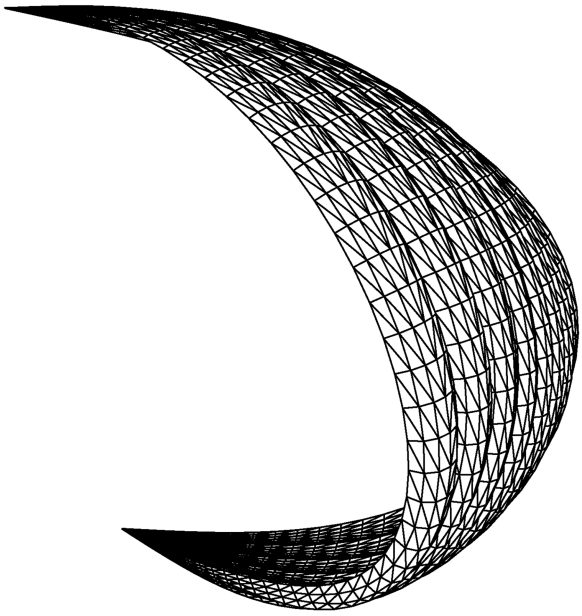

Fig. 8 One-half of a fundamental of an equilibrium configuration with fourfold symmetry (eight gores, one-eighth of a complete balloon); the complete balloon is shown in Fig. 9.

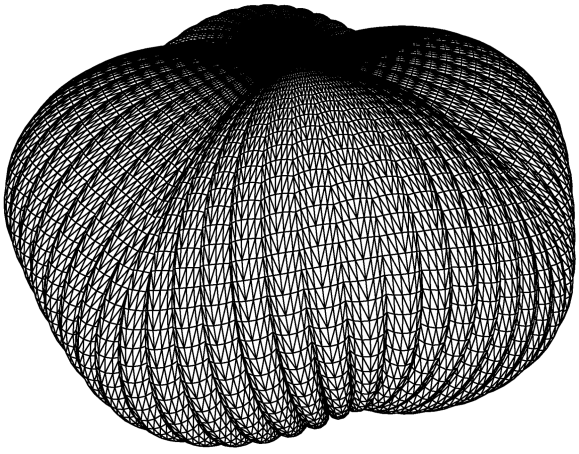

Fig. 9 Equilibrium configuration with fourfold symmetry.

identical to the cyclically symmetric shape found in the case with $p = \frac{1}{2}$.

Even though the Endeavour was inflated at a pressure much higher than $P_0 = 200$ Pa and used different materials, there is a striking similarity between the images in Figs. 1b, 1c, 9, and 10.

VII. Conclusions

If a fully inflated cyclically symmetric balloon configuration is unstable, then it must assume an alternate stable asymmetric configuration. We explored this phenomena using an Euler-elastica constant-bulge-angle pumpkin balloon similar in size to Julian Nott's Endeavour balloon. By introducing linear constraints to handle the problem of self-contact, we were able to solve a formulation of the balloon problem and calculate asymmetric equilibria, including those with fourfold and threefold symmetry. Our computed shapes bear a striking resemblance to the asymmetric shapes that have been observed in ground inflation tests of small balloons intentionally fabricated with excess material and the Endeavour configurations (see Fig. 1). In addition, we carried out a stability analysis of a class of Euler-elastica constant-bulge-angle pumpkin balloons and a comparable class of Euler-elastica constant-bulge-radius pumpkin balloons. We found that an Endeavour-like (EECBA) design was much more likely to have an unstable, fully inflated, cyclically symmetric equilibrium than an Euler-elastica constant-bulge-radius pumpkin balloon of comparable size. Our stability results on the EECBA pumpkin balloons studies are in close agreement with Calledine's [1] stability work. Although reducing the number of gores from 64 to 60 was a quick fix for the obvious Endeavour deployment difficulties, similar, but much more subtle, difficulties are yet to be resolved for the deployment of large NASA ultra-long-duration pumpkin balloons. Although it is clear that it would be impossible for a large pumpkin balloon that is based on an unstable design to achieve a cyclically symmetric configuration at float, it has yet to be demonstrated that a stable design will consistently deploy during a nominal ascent. Moreover, even if such a balloon were to deploy, other hurdles due to the midlatitude long-duration aspects of flight will need to be overcome. Uncertainties that arise with our predictions come from the fact that the film for the gas envelope for NASA's ULDB is nonlinearly viscoelastic and that cost-effective fabrication introduces significant structural imperfections. The former is difficult to include accurately in the analysis. The latter is impossible to accurately account for in a deterministic way. Both of these aspects, however, can be treated satisfactorily using the tools and techniques used in this paper. What is needed is a series of analyses that bound the problem. Both viscoelasticity and the effect of structural imperfections require exploratory sensitivity analysis before settling on a design class for which safe design guidance can be provided.

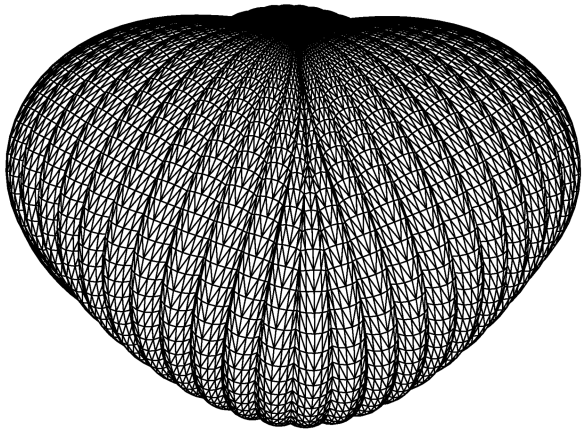

Fig. 10 Equilibrium configuration with threefold symmetry.

Acknowledgments

The first two authors were supported by NASA award NAG5-5353. The authors would like to thank Julian Nott for providing the Endeavour photographs. The authors are grateful for the comments provided by the reviewers.

References

[1] Calledine, C. R., "Stability of the Endeavour Balloon," *Buckling of Structures*, Elsevier, New York, 1988, pp. 133–149.

[2] Lennon, A., and Pellegrino, S., "Stability of Lobed Inflatable Structures," 41st AIAA/ASME/ASCE/AHS/ASC Structural Dynamics, and Materials Conference and Exhibit, Atlanta, GA, AIAA Paper 2000-1728, 2000.

[3] Baginski, F., "On the Design and Analysis of Inflated Membranes: Natural and Pumpkin Shaped Balloons," *SIAM Journal on Applied Mathematics*, Vol. 65, No. 3, 2005, pp. 838–857.

[4] Baginski, F., Brakke, K., and Schur, W., "Cleft Formation in Large Pumpkin Balloons," *Advances in Space Research*, Vol. 37, 2006, pp. 2070–2081.

[5] Baginski, F., Brakke, K., and Schur, W., "Stability of Cyclically Symmetric Strained Pumpkin Balloon Configurations and the Formation of Undesired Equilibria," *Journal of Aircraft*, Vol. 43, No. 5, 2006, pp. 1414-1423.

[6] Smalley, J. H., "Development of the e-Balloon," National Center for Atmospheric Research, AFCRL-70-0543, Boulder, CO, June 1970.
[7] Baginski, F., and Schur, W., "Undesired Equilibria of Self-Deploying Pneumatic Envelopes," (submitted for publication).
[8] Baginski, F., and Schur, W., "Structural Analysis of Pneumatic Envelopes: A Variational Formulation and Optimization-Based Solution Process," *AIAA Journal*, Vol. 41, No. 2, Feb. 2003, pp. 304–311.
[9] Brakke, K., "The Surface Evolver," *Experimental Mathematics*, Vol. 1, No. 2, 1992, pp. 141–165.
[10] Wakefield, D., "Numerical Modeling of Pumpkin Balloon Instability," 5th ATIO and 16th Lighter-than-Air and Balloon Systems Conferences, Crystal City, VA, AIAA Paper 2005-7445, 2005.
[11] Press, W. P. , Flannery, B. P., Teukolsky, S. A., and Vetterling, W. T., *Numerical Recipes in C*, 2nd ed., Cambridge Univ. Press, Cambridge, England, U.K., 1992.
[12] Libai, A., and Simmonds, J. G., *The Nonlinear Theory of Elastic Shells*, 2nd ed., Cambridge Univ. Press, Cambridge, England, U.K., 1998.
[13] Schur, W. W., and Jenkins, C. H., "Deployment Destiny, Stable Equilibria, and the Implications for Gossamer Design," 43nd AIAA/ASME/ ASCE/AHS/ASC Structures, Structural Dynamics and Materials Conference and Exhibit, Denver, CO, AIAA Paper 2002-1205, 2002.
[14] Smith, M. S., and Rainwater, E. L., "Optimum Designs for Super-Pressure Balloons," *Advances in Space Research*, Vol. 33, 2004, pp. 1688–1693.